NANO LETTERS

Letter

pubs.acs.org/NanoLett

Bubble-Pen Lithography

Linhan Lin,[†,‡,▽] Xiaolei Peng,[‡,▽] Zhangming Mao,[§] Wei Li,[‡,∥] Maruthi N. Yogeesh,[∥] Bharath Bangalore Rajeeva,[‡] Evan P. Perillo,[⊥] Andrew K. Dunn,[⊥] Deji Akinwande,[‡,∥] and Yuebing Zheng*[,†,‡]

[†]Department of Mechanical Engineering, The University of Texas at Austin, Austin, Texas 78712, United States

[‡]Materials Science & Engineering Program and Texas Materials Institute, The University of Texas at Austin, Austin, Texas 78712, United States

[§]Department of Engineering Science and Mechanics, The Pennsylvania State University, University Park, Pennsylvania 16802, United States

[∥]Microelectronics Research Centre, The University of Texas at Austin, Austin, Texas 78758, United States

[⊥]Department of Biomedical Engineering, The University of Texas at Austin, Austin, Texas 78712, United States

Supporting Information

ABSTRACT: Current lithography techniques, which employ photon, electron, or ion beams to induce chemical or physical reactions for micro/nano-fabrication, have remained challenging in patterning chemically synthesized colloidal particles, which are emerging as building blocks for functional devices. Herein, we develop a new technique - bubble-pen lithography (BPL) - to pattern colloidal particles on substrates using optically controlled microbubbles. Briefly, a single laser beam generates a microbubble at the interface of colloidal suspension and a plasmonic substrate via plasmon-enhanced photothermal effects. The microbubble captures and immobilizes the colloidal particles on the substrate through coordinated actions of Marangoni convection, surface tension, gas pressure, and substrate adhesion. Through directing the laser beam to move the microbubble, we create arbitrary single-particle patterns and particle assemblies with different resolutions and architectures. Furthermore, we have applied BPL to pattern CdSe/ZnS quantum dots on plasmonic substrates and polystyrene (PS) microparticles on two-dimensional (2D) atomic-layer materials. With the low-power operation, arbitrary patterning and applicability to general colloidal particles, BPL will find a wide range of applications in microelectronics, nanophotonics, and nanomedicine.

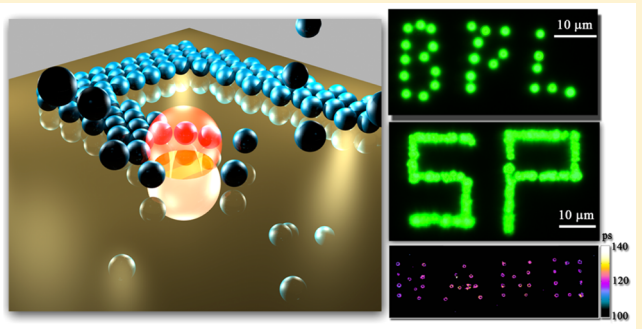

KEYWORDS: *Microbubbles, photothermal effect, patterning, colloidal particles, quantum dots, two-dimensional materials*

Lithography[1−4] and chemical synthesis[5,6] are considered as two primary strategies for nanofabrication. Photolithography has remained as the driving force for semiconductor industry. However, its resolution is reaching an ultimate limit. E-beam lithography and ion-beam lithography feature high resolution and arbitrary patterning, however, are limited by high cost and low throughput. Chemical synthesis has advantages in both low cost and precise control of compositions, sizes, and shapes of nanomaterials. With their precisely tailorable properties down to the atomic level, colloidal micro/nano-particles are promising as building blocks for functional devices.[7−9] However, the device applications require the patterning of particles on solid-state substrates. For this purpose, a wide range of techniques have been developed, including self-assembly,[10−14] Langmuir−Blodgett (LB) method,[15] dip-pen nanolithography,[16,17] polymer pen lithography,[18] and contact-printing.[19]

Optical tweezers have been proved effective in manipulating the colloidal micro/nano-particles in solutions.[20−22] Despite its capability of offering remote, real-time, and versatile manipulations of colloidal particles, conventional optical tweezers require high laser power (100 mW/μm^2) that can damage the colloidal particles and have remained challenging to immobilize the particles onto the substrates. Although a combination of optical trapping and convective fluid flow leads to immobilized particles of a single type of featureless close-packed aggregates on the substrates upon the solvent evaporation,[23] there remains a critical need for new light-based techniques that can create the arbitrary patterns of colloidal particles immobilized on the substrates. Recently, Feldman and his co-workers used the optical tweezers to trap the metallic nanoparticles at the

Received: November 5, 2015
Revised: December 15, 2015

DOI: 10.1021/acs.nanolett.5b04524
Nano Lett. XXXX, XXX, XXX−XXX

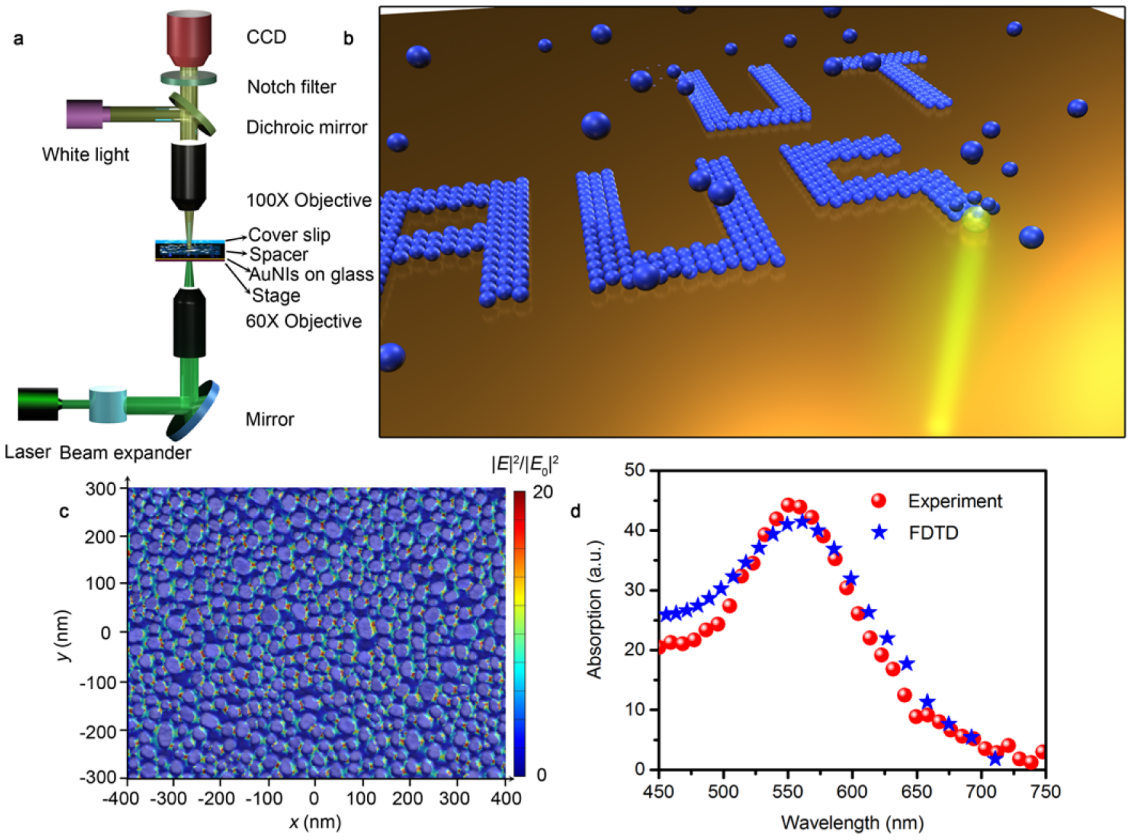

Figure 1. Working principle of BPL. (a) An overview of the experimental setup for BPL. (b) Schematic illustration of the pattern-writing process using an optically controlled microbubble on a plasmonic substrate. The small blue spheres are colloidal particles. (c) An overlay of scanning electron microscopy (SEM) image and simulated electric field distributions of quasi-continuous Au nanoislands (AuNIs). (d) Simulated and experimental absorption spectra of the AuNIs substrate.

resonance wavelength, guide them to the substrate, and bind the particles via van der Waals attraction to the substrate.[24] Optoelectronic tweezers represent another milestone in extending the capability of optical tweezers.[25−28] Based on the optically patterned virtual electrodes on a photosensitive substrate, optoelectronic tweezers can grab and immobilize colloidal particles on the surface of hydrogenated amorphous silicon.[29]

I. Working Principle of BPL. Herein, we have developed BPL to optically write arbitrary patterns of colloidal particles on the substrates. In BPL, an optically controlled microbubble is generated to capture and immobilize colloidal particles on the plasmonic substrates through the coordinated actions of Marangoni convection, surface tension, gas pressure, and substrate adhesion in the substrate−bubble−solution system. The irradiation of a plasmonic substrate with a focused laser beam at the plasmon resonance wavelength generates a microbubble at the substrate−solution interface. Due to the plasmon-enhanced photothermal effects, the bubbles of variable sizes can be generated at a significantly reduced power. We can generate bubbles down to 1 μm in diameter, which are much smaller than the microbubbles (diameter in the range of 50−100 μm) commonly used in microfluidic devices for manipulation of particles.[30−32]

Figure 1a illustrates the experimental setup for BPL. A laser beam is focused onto the plasmonic substrate by a high-magnification objective from the bottom of the sample. An optical microscope with a white light source, objectives, and a CCD is integrated into the system for real-time monitoring of the patterning process. Colloidal particles suspended in deionized (DI) water were sandwiched between a plasmonic substrate and a coverslip with a spacer of 120 μm. As illustrated in Figure 1b, a microbubble is generated on the plasmonic substrate upon the irradiation of a laser beam of 2 μm in diameter due to water vaporization from the plasmon-enhanced photothermal effects.[33,34] The colloidal particles are dragged toward the microbubble, trapped on the bubble/water interface and eventually immobilized on the substrate. By controlling the laser beam, we can move the microbubble to create patterns of particles dictated by the trajectories of bubble movement.

The optical generation of microbubbles at the solid−water interface using plasmonic substrates consisting of Au nanoparticles was reported previously.[33,35,36] Herein, we employ the plasmonic substrates consisting of AuNIs, which are tuned to match their plasmon resonance wavelength with the laser wavelength (532 nm) and to have the high nanoparticle density in order to minimize the critical optical power for the bubble generation (see Figure S1). The typical plasmonic substrate has Au nanoparticles of 20−40 nm in diameters and 5−10 nm in interparticle distances with the particle density of 1×10^{11} particles/cm^2 (Figure 1c), which is much higher than the particle density in the plasmonic substrates in previous work.[33,35] As shown by the simulated electromagnetic field distributions over the SEM image of the AuNIs (Figure 1c), the laser irradiation leads to the high-density electromagnetic "hot spots" that arise from the strong near-field coupling between the neighboring Au nanoparticles. The network of "hot spots" on the AuNIs allows the spatially continuous generation and

DOI: 10.1021/acs.nanolett.5b04524
Nano Lett. XXXX, XXX, XXX−XXX

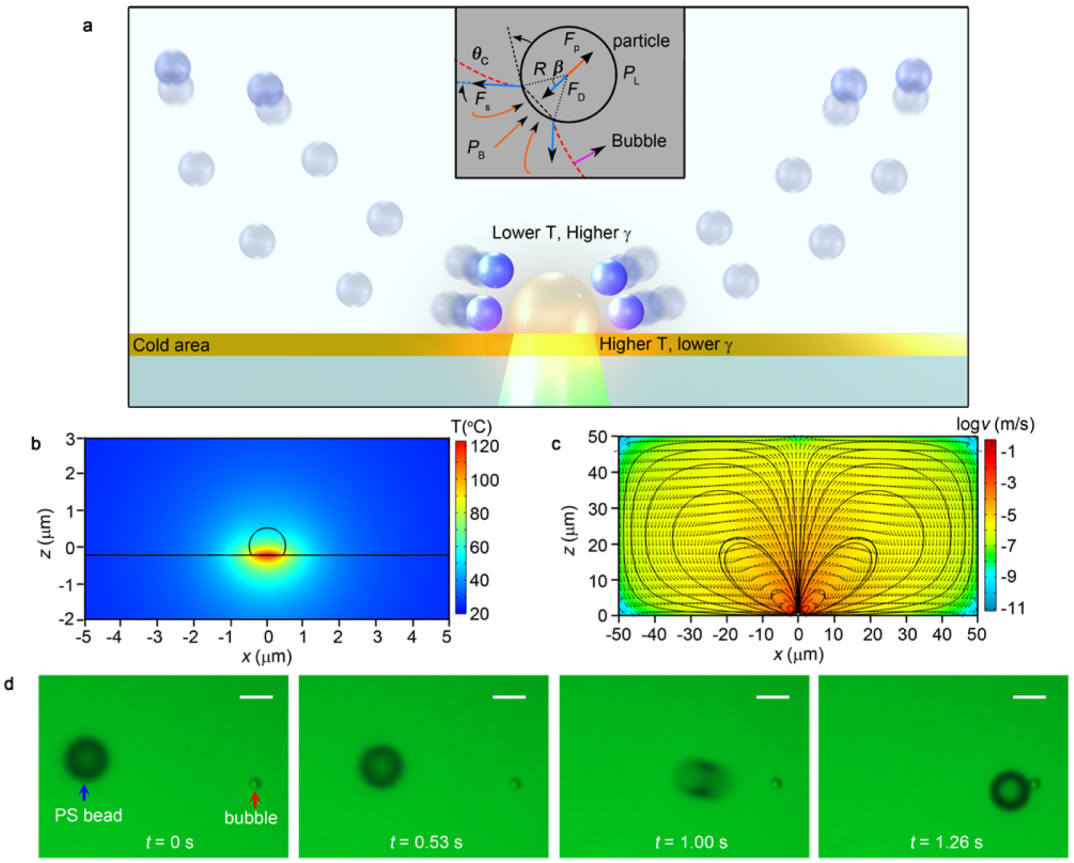

Figure 2. Particle trapping at a microbubble that is generated through the plasmon-enhanced photothermal effects. (a) Schematic illustration (in a cross-sectional view) of the particle-trapping mechanism by a single microbubble. The blue spheres indicate the suspended particles in the DI water. The particles follow the convective flow due to the frictional force. The inset shows the force distribution when a particle is trapped by the microbubble (indicated as the red dash line). P_B and P_L indicate the pressure in the bubble and liquid, respectively, which introduce a net force of F_P pushing the particle outward. The surface tension F_S introduce a drag force F_D. (b) Simulated temperature distribution around a 1 μm bubble in a cross-sectional view. (c) Simulated flow velocity distribution around a 1 μm bubble with logarithmic scale in a cross-sectional view. The black lines indicate streamlines of the convective flow. (d) Time-resolved trapping process of a single 5.31 μm PS bead by a 1 μm bubble. Scale bar: 5 μm.

movement of microbubbles for the arbitrary patterning. Both simulated and experimental absorption spectra (Figure 1d) reveal that the plasmon resonance peak wavelength of the AuNIs matches the laser wavelength, which significantly enhances the light absorption and photothermal effects for the low-power bubble generation.

In BPL, both natural convection and Marangoni convection are responsible for the particle trapping at the microbubbles. The former is caused by the temperature gradient on the plasmonic substrate. The latter is induced by the surface-tension gradient along the microbubble surface (Figure 2a). The convective flow drags the colloidal particles down to the plasmonic substrate, and the in-plane drag force drives the particles toward the microbubble. The trapping occurs when a particle touches the microbubble, as shown in the inset of Figure 2a. The surface tension force F_S at the gas/liquid interface leads to an effective drag force F_D, which attracts the particle toward the microbubble. The pressure inside the microbubble, which can reach 3.4 bar for the 1 μm bubble,[35] is much higher than the pressure in water, which can be treated as atmospheric pressure. The balance is achieved when the ratio between F_D and F_P becomes 1:[32]

$$\frac{F_D}{F_P} = \frac{R_B}{R}\frac{\sin(|\theta_C - \beta|)}{\sin\beta} = 1 \quad (1)$$

where R_B is the radius of the microbubble, F_P is the force induced by the gas/liquid pressure difference, R is the radius of the colloidal particles, θ_C is the contact angle between the particle and the bubble, and β is the half-central angle.

We used computational fluid dynamics (CFD) simulations to obtain the temperature distribution around a 1 μm bubble (Figure 2b) when the substrate is illuminated by a focused laser beam with a diameter of 2 μm (see Figure S2) and power density of 0.56 mW/μm^2 (measured at the focus point of the objective). The resultant bottom-to-top temperature difference of ~60 °C creates the surface tension gradient along the bubble surface. The flow velocity distribution around this microbubble is displayed in Figure 2c, with a maximum flow velocity of ~0.3 m/s at the gas/liquid interface (also see Figure S3 for the CFD simulations of a 3 μm bubble). The flow velocity decreases when the distance from the microbubble is increased. It ranges from 1 to 100 μm/s at the distances of 15−5 μm. Due to the convective flow, the particles are dragged toward the microbubble according to Stokes' law:

$$F_d = 6\pi\mu R\nu(R) \quad (2)$$

where μ is the dynamic viscosity of the solution, and $\nu(R)$ is the flow velocity of solvent relative to the particles, which is also dependent on R. As shown in Figure 2c, the larger particles have the mass center farther away from the substrate surfaces,

DOI: 10.1021/acs.nanolett.5b04524
Nano Lett. XXXX, XXX, XXX−XXX

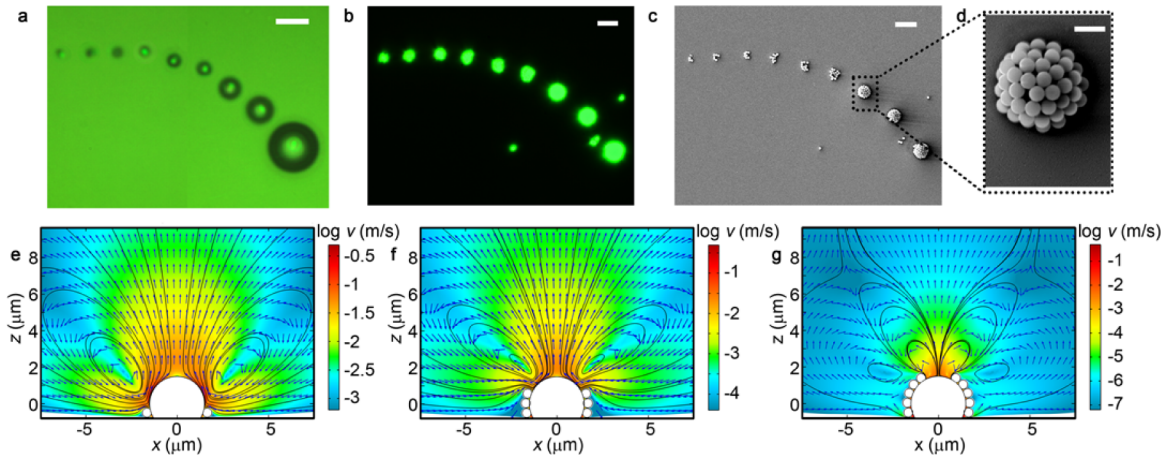

Figure 3. Patterning of the PS beads on the substrate at different laser powers. (a) Optical micrographs of a series of microbubbles generated with different laser power densities: 0.56, 0.64, 0.68, 0.77, 0.83, 0.91, 0.97, 1.04, and 1.12 mW/μm^2 (from small to large bubbles). (b) Dark-field optical micrographs and (c) SEM image of the series of patterned 540 nm PS beads generated with corresponding power densities in panel a. (d) High-magnification image of the 3D hollow structure formed at a laser power density of 0.97 mW/μm^2. The flow velocity distribution (logarithmic scale) around a 3 μm microbubble in a cross-sectional view when (e) one layer, (f) three layers, and (g) five layers of 540 nm PS beads are trapped at the gas/liquid interface. Scale bar: (a–c) 5 μm; (d) 1 μm.

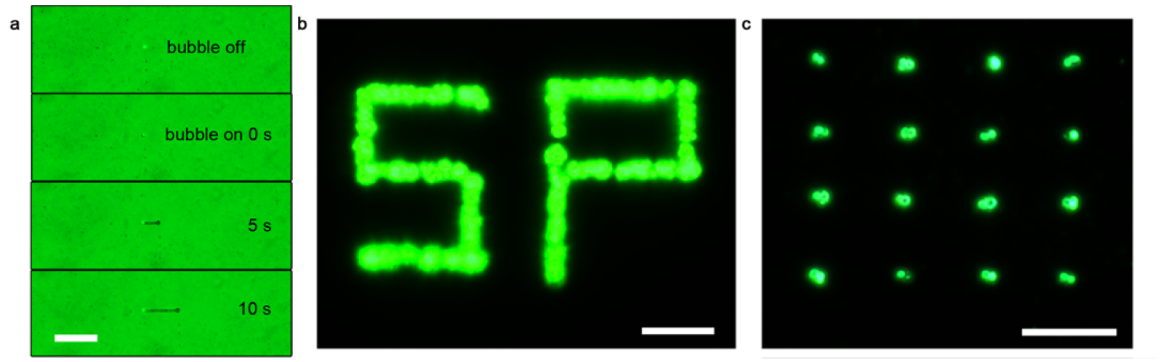

Figure 4. Patterning of PS beads of different sizes on the plasmonic substrates. (a) Time-resolved process for continuous writing of a straight-line pattern of 540 nm PS beads on the AuNIs substrate. (b) Dark-field optical image of the "SP" pattern of 540 nm PS beads. (c) Dark-field optical image of the 4 × 4 array of 3D hollow structures of 60 nm PS beads. Scale bar: (a) 50 μm; (b,c) 10 μm.

experiencing a different flow velocity from the smaller particles. At a constant mass density, the acceleration of the particles is estimated as

$$a \propto \mu R^{-2} \nu(R) \tag{3}$$

We measured the particle-trapping speed by recording the time-resolved trapping processes of single PS beads with diameters of 540 nm, 0.96 μm, and 5.31 μm (Figure 2d and Figure S4). A traveling distance of ~20 μm is used to estimate the average trapping speed. The 5.31 μm PS bead exhibits a speed of 18.1 μm/s. The drag force and trapping speed depend on the distance between the particle and the microbubble. There is a dramatic increase of the trapping speed when the particle approaches the microbubble (Figure 2d), indicating that the relative velocity ν dominates the trapping process. In addition, the smaller PS beads experience higher trapping speed, i.e., 27.5 μm/s for the 0.96 μm PS and 31.1 μm/s for the 540 nm PS, respectively (also see Supporting Movie 1 for the real-time trapping).

II. Patterning of PS Micro/Nanoparticles on Plasmonic Substrates. We exploit the plasmon-enhanced photothermal effects, which improve the adhesion between the PS beads and the substrate, to immobilize the bubble-trapped particles on the substrates for particle patterning. Figure 3a shows the optical micrographs of the variable microbubbles generated under the light illumination with different power densities (also see Figure S5 and Supporting Movies 2 and 3 for the expansion and shrinkage of the microbubble). Although the generation of two or more bubbles simultaneously is possible by including an optical imaging system in the setup (Figure S6), the bubble pattern in Figure 3a was generated in series by translating the sample stage and recorded in sequence. The smallest bubble with a diameter of 1 μm is generated at the laser power density of 0.56 mW/μm^2. An increase in the optical power density enlarges the bubbles because an increased amount of water steam was generated, and air molecules diffused into the bubbles. As shown in Figure 3b,c, the 540 nm PS beads can be immobilized on the substrate by the bubbles, leading to the different patterns. At the lowest optical power density, three PS beads form a cluster with 2D configuration. When the power density is increased to 0.97 mW/μm^2, a large bubble with a diameter of >3 μm leads to a three-dimensional (3D) hollow structure of the beads on the substrate (Figure 3d), revealing that the trapped PS beads are aligned along the whole gas/liquid interface. Besides the bubble size, the patterns of beads

DOI: 10.1021/acs.nanolett.5b04524
Nano Lett. XXXX, XXX, XXX−XXX

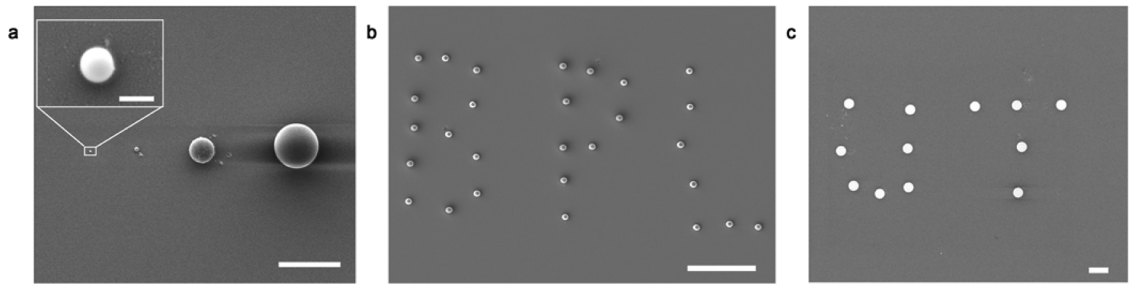

Figure 5. Patterning of PS beads at single-particle resolution. (a) Patterning of single PS beads with different sizes: 540 nm, 0.96 μm, 5.31 μm, and 9.51 μm, respectively (from left to right). (b) SEM image of the "BPL" pattern of 0.96 μm PS beads. (c) SEM image of the "UT" pattern of 5.31 μm PS beads. Scale bar: (a–c) 10 μm; inset of (a) 500 nm.

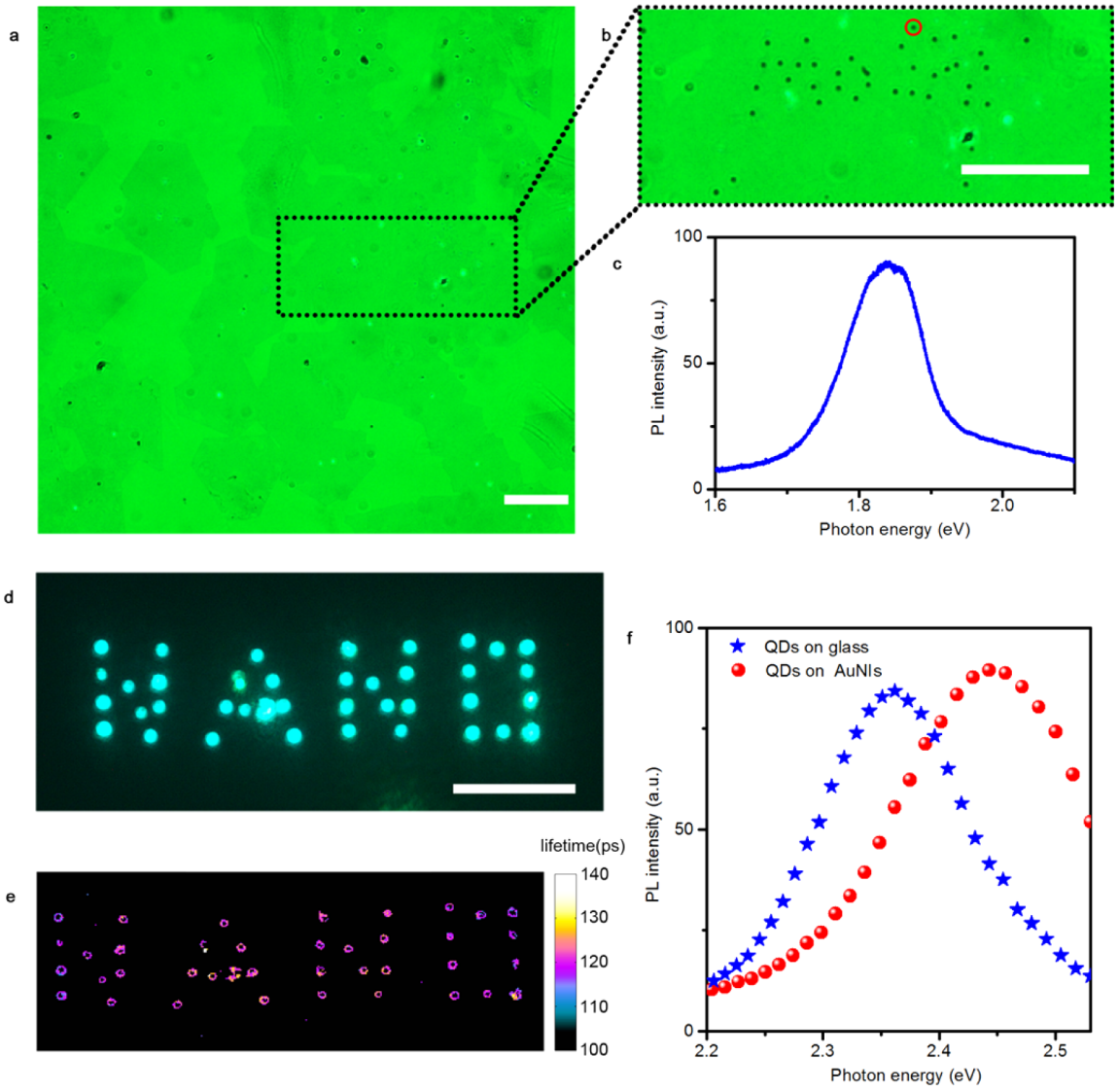

Figure 6. Versatility of BPL in patterning 2D materials and quantum dots. (a) Optical micrograph of the 2D MoS_2 monolayers on the AuNIs substrate. (b) Optical micrograph of the "MoS_2" patterns of individual 0.96 μm PS beads written on the 2D MoS_2 monolayer. (c) The PL spectrum of the MoS_2 recorded from the regime with a single PS bead, as indicated by the red circle in (b). (d) Fluorescence image of the "NANO" pattern of 6 nm CdSe/ZnS quantum dots on the AuNIs. (e) Fluorescence lifetime image of the patterned CdSe/ZnS quantum dots as shown in panel d. (f) PL spectra of the quantum dots patterned on the plasmonic substrate and of the quantum dots on the glass substrate. Scale bar: 50 μm.

also depend on the concentration of the beads in the solution and the laser irradiation time.

We apply CFD simulations to gain an insight into the formation mechanism of the 3D hollow structures of PS beads. As illustrated in Figures 3e–g, the convective flow drags the beads toward the bubble/substrate interface and generates the 3D hollow structure by the "bottom-up" layer-by-layer stacking. Such a stacking process is enabled by the fact that the initially

DOI: 10.1021/acs.nanolett.5b04524
Nano Lett. XXXX, XXX, XXX–XXX

trapped beads at the bubble surface block the Marangoni stress and modify the convective flow distributions in a way that the convective flow points toward the upper part of the bubble. In addition, the trapped beads reduce the surface tension gradient and thus the flow velocity along the bubble surface. However, a reverse convective flow occurs when the bubble traps five layers of beads (Figure 3g). The reverse flow pushes the free beads in suspension away from the trapped ones. The velocity around the microbubble is 4−5 orders of magnitude lower than that before the beads are trapped, indicating that the trapping process stops once the bubble surface is covered with beads. The 3D hollow structures are generated when the microbubbles are significantly larger than the beads. When the bubbles and beads have comparable sizes, one-layer or two-layer 2D aggregates are generated due to the limited surface area of the bubbles (Figure S7).

Taking advantage of the quasi-continuous AuNIs as the plasmonic substrate, we have achieved continuous writing of the patterns of colloidal particles on the substrate by scanning the laser beam or translating the sample stage. Figure 4a illustrates the writing process for a straight line of 540 nm PS beads at the laser power density of 0.56 mW/μm^2 (see Supporting Movie 4 for the real-time continuous writing process). At the lower power density (top panel of Figure 4a), no microbubble was generated. Still, the optically generated temperature gradient led to the natural convection, moving the PS beads upward at the illuminated area without trapping and immobilization (see Supporting Movie 5 and Figure S8 for the comparison between the natural convection before the bubble generation and the trapping and patterning of 0.96 μm PS bead after the formation of the microbubble). When the laser power density was increased to the critical value, a microbubble was generated, and the PS beads were collected and immobilized on the illuminated spot (second panel in Figure 4a). During the translation of the sample stage, the original microbubbles disappeared, leaving behind the immobilized beads, and new ones were generated at the new locations to trap and immobilize the beads, leading to the patterns of the beads that follow the trails of the bubbles (third and fourth panels in Figure 4a). As an example, we wrote the "SP" pattern of 540 nm PS beads using a 1 μm microbubble (Figure 4b). Since the sizes of the PS beads and the microbubble are comparable, the patterns feature a 2D configuration (see Figure S7). Due to the high trapping and immobilization efficiencies, the microbubble allows the rapid scanning of the laser beam and the high-throughput patterning at a large scale.

In another example, Figure 4c shows the 4 × 4 arrays of the PS beads with a diameter of 60 nm. Since the beads (60 nm) are much smaller than the microbubble, the 3D hollow structures are obtained (see Figure S9). CFD simulations support the formation of the 3D hollow structures (Figure S10). Moreover, the 3D hollow structure can be continuously written on the substrate, leading to the hollow-ridge patterns of the beads (Figure S11). Such 3D hollow structures may find applications in omnidirectional optical devices, wide-angle-view imaging, and microlenses.[37−39]

We evaluate the BPL resolution based on our current experimental setup. As shown in Figure 5a, the patterning of single PS beads with size ranging from 540 nm to 9.51 μm has been achieved. Individual beads can also be patterned into "BPL" (bead diameter: 0.96 μm) and "UT" (bead diameter: 5.31 μm) logos (Figures 5b,c). With the capability of patterning single beads, BPL can be a pivotal tool in the single-particle sensing[40] and single-cell analysis.[41] It will be interesting to test the ultimate resolution of BPL, which will require better imaging and concentration control for the nanoparticles below 100 nm.

III. Patterning of PS Microparticles on 2D Atomic-Layer Materials. BPL is applicable to patterning particles on the surfaces beyond the plasmonic substrates. We have achieved arbitrary patterning of the PS beads on 2D atomic-layer materials. For the demonstration, we grew the MoS_2 atomic monolayers with chemical vapor deposition (CVD) and transferred them onto the AuNIs substrate (Figure 6a). As illustrated in Figure 6b, the "MoS_2" patterns of individual PS beads with a diameter of 0.96 μm are created on the MoS_2 monolayer using BPL. In Figure 6c, the photoluminescence (PL) spectrum taken from the patterned area, as indicated by the red circle in Figure 6b, reveals that there is no damage to the 2D monolayer during patterning by BPL. The subnanoscale thickness (6.7 Å) of the 2D monolayer with a thermal conductivity of 34.5 W/mK[42] makes it possible to generate microbubbles on its top. In principle, BPL is applicable to a variety of particles and 2D materials. By synergizing the unique properties of 0D and 2D systems, the heterostructures of micro/nanoparticles and 2D materials could exhibit novel functions for different applications. In addition, the particles can work as the masks for further patterning of a 2D monolayer through selective etching or deposition of new materials.

IV. Patterning of Quantum Dots on Plasmonic Substrates. To further demonstrate the versatility of BPL, we have accomplished its use for arbitrary patterning of quantum dots with a size much smaller than that of the PS beads. As an example, we used the CdSe/ZnS core/shell quantum dots with a diameter of 6 nm for the BPL. As shown in Figure 6d, the "NANO" pattern of the quantum dots were created on the AuNIs substrate. We measured the fluorescence lifetime of the patterned quantum dots using time-correlated single-photon counting technique (Figure 6e). An average lifetime of ∼120 ps for the patterned quantum dots is much shorter than that of the original quantum dots (8.1 ns; see Figure S12). The reduced lifetime reveals that the strong plasmon-exciton interactions within the coupled system consisted of quantum dots and plasmonic substrate.[43] The plasmon-exciton coupling is further confirmed by PL spectra of the quantum dots, which made a blueshift from 2.35 to 2.45 eV upon their patterning on the AuNIs (Figure 6f). With their well-controlled and highly tailorable nanostructures, the patterned quantum dots on plasmonic substrates can not only serve as platforms for the fundamental study of plasmon-exciton coupling, but also find applications in nanophotonics and optoelectronics such as ultrafast light sources.

Conclusion. In summary, we have developed a versatile lithography technique known as BPL for arbitrary patterning of colloidal particles on solid-state substrates using optically controlled microbubbles. Through combining experiments and numerical simulations, we have established that the coordinated actions of Marangoni convection, surface tension, gas pressure, and substrate adhesion hold the key to the trapping and immobilization of particles in BPL. With the plasmon-enhanced photothermal effects on the properly engineered plasmonic substrates, BPL can operate efficiently in a continuous-scanning mode and at low laser power. The versatility of BPL is reflected in its capability of writing arbitrary patterns of single and clusters of particles in 2D or 3D configurations and in its applicability to various colloidal

DOI: 10.1021/acs.nanolett.5b04524
Nano Lett. XXXX, XXX, XXX−XXX

particles and substrates beyond plasmonic nanostructures. The high tunability of bubble size, substrate temperature, and flow convention in BPL has significantly enriched the configurations of particles in the patterns. The ultimate resolution of BPL has remained to be tested.

It is worth noting that the current study exploits the photothermal effects for the immobilization of particles on the substrates, which is applicable to thermoresponsive particles like PS beads and CdSe/ZnS quantum dots with polymer coating. We believe that surface-functionalization methods can be employed to enhance the substrate−particle interactions for the immobilization of a wider range of particles, including electrostatic attraction and chemical recognition. Besides serving as a platform for fundamental research on colloidal nanoscience, the patterned particles on AuNIs substrates can be used as prepared or transferred to different substrates for functional device applications. For the former, the plasmonic effects can be exploited to enhance the performance of the particles such as the shortened fluorescence lifetime of quantum dots on the AuNIs substrates. The capability of patterning colloidal particles on 2D materials opens up new opportunities for new functional hybrid materials and devices that benefit from the synergistic integration of 0D and 2D materials.

Methods. *Materials Information.* To fabricate the optimized AuNIs plasmonic substrate, a 4 nm Au film was deposited on the glass substrate with thermal deposition (Denton thermal evaporator) at a base pressure of 9×10^{-6} Torr, followed by the thermal annealing at 550 °C for 2 h. The PS beads with sizes of 60 nm (1 wt %), 540 nm (9.83 wt %), 0.96 μm (10 wt %), 5.31 μm (9.6 wt %) and 9.51 μm (10.08 wt %) were ordered from Bangs Laboratories, Inc. For the continuous patterning, the 540 nm PS solution was diluted with DI water (1:1,000, v/v), and the 60 nm PS solution was diluted with a volume ratio of 1:10. For single-particle patterning, all the particle solutions were diluted with DI water (1:10 000, v/v). The CdSe/ZnS quantum dots were purchased from Life Technology Inc. (Qdot525 streptavidin conjugate). The 6 nm CdSe/ZnS core/shell quantum dots have polymer coating and biomolecules on the outer shell, leading to a total size of 15−20 nm. The quantum dots were diluted using DI water (1:30, v/v) for the patterning process. MoS_2 monolayers were grown by a standard vapor transfer growth process and transferred to the AuNIs substrates. Briefly, MoO_3 (15 mg) and sulfur (1 g) powder were loaded in separate alumina crucibles and heated independently using a heating tape. At a base pressure of <10 mTorr, the tube was purged with pure N_2 gas at 200 sccm for 4 cycles. After that, the tube was filled with N_2 to 1 atm pressure at 10 sccm. The furnace was heated to 850 °C for the growth of MoS_2 on SiO_2 surfaces with a heating rate of 50 °C/min. The growth process lasts for 5 min. To transfer MoS_2 from SiO_2 to the AuNIs substrate, PMMA was spin-coated on the top of 2D monolayers. The SiO_2 was then etched away with sodium hydroxide solution (NaOH, 2M, 80 °C), and the PMMA-supported MoS_2 was transferred to the AuNIs substrate. The transferred sample was stored in a desiccator and baked at 180 °C for 2 min to improve the adhesion. After the selective removal of PMMA in acetone, MoS_2 monolayers remain on the AuNIs substrate.

SEM Characterization. The high-resolution SEM image of the AuNIs in Figure 1 was taken using the Hitachi S5500 SEM/STEM system. The other SEM images were taken using the FEI Quanta 650 ESEM.

Numerical FDTD Simulations. The 3D electromagnetic simulations were performed with a commercial software (FDTD Solutions, Lumerical Solutions). The geometry of the AuNIs was imported from the high-resolution SEM images, which was defined with a fine mesh size of 1 nm. The optical constants of Au were taken from Johnson and Christy,[44] and the refractive index of the glass substrate is set as 1.52. A broadband plane wave was used to illuminate the AuNIs. Perfectly matched layers were utilized as the boundary conditions for all directions. The electromagnetic field distributions were recorded at an excitation wavelength of 532 nm, which matches the laser wavelength in our experiments.

Numerical CFD Simulations. CFD simulations were conducted using a finite-element solver (COMSOL Multiphysics). For simplicity, a 2D axisymmetric model comprising of a glass substrate, PS beads, a stream microbubble, and water was established. The physics involved includes fluid dynamics in laminar flow (water and stream) and conjugate heat transfer in solids (glass substrate and PS beads) and fluids (water and stream). Three kinds of couplings were considered in the simulations, including nonisothermal flow multiphysics coupling, Marangoni effect multiphysics coupling, and gravity that introduces buoyant force. The boundary conditions considered for the heat transfer are composed of a boundary heat source at the glass/stream bubble interface (to model the laser heating) and room temperature for other boundaries. For the laminar flow physics, the water/stream bubble interface was set as a slip interior wall, while the other boundaries were set as nonslip walls.

Optical Characterizations. The absorption spectra of the AuNIs were taken using the Ocean Optics spectrometer (HR4000CG-UV-NIR). The PL spectra of quantum dots were taken under a micro Raman system (Witec micro-Raman spectrometer Alpha 300) with a 488 nm laser as the excitation source. The PL spectrum of the MoS_2 monolayer was recorded with a micro Raman system using a 532 nm laser as the excitation source. The fluorescence lifetime imaging of the quantum dots was performed with time-correlated single-photon counting, which includes the femtosecond titanium:sapphire laser tuned to 800 nm (~200 fs) (Mira 900, Coherent), galvo scanning mirrors (6215H, Cambridge Tech.), and a GaAsP photomultiplier tube (PMT) (H7422PA-40, Hamamatsu) in nondescanned detection scheme. The output current of the PMT is amplified using a preamplifier (HFAC- 26, Becker and Hickl GmbH) prior to reaching the photon counting board (SPC-150, Becker and Hickl GmbH). Fluorescence lifetimes were recorded with a 20 ps time resolution and a pixel integration time of 5 ms using an average laser power of 1 mW. Lifetime fitting was performed with the least-squares method using a model of a single exponential decay convolved with a Gaussian impulse function. The resultant lifetime image was threshold-based on intensity to remove the background signals from the AuNIs substrate. Data points with fewer than 500 photons were removed from the fitting, and the fittings with χ^2 value less than 2 were discarded to ensure a high fitting quality.

■ ASSOCIATED CONTENT

Supporting Information

The Supporting Information is available free of charge on the ACS Publications website at DOI: 10.1021/acs.nanolett.5b04524.

DOI: 10.1021/acs.nanolett.5b04524
Nano Lett. XXXX, XXX, XXX−XXX

SEM and transmission spectra of different AuNI substrates (Figure S1), optical image of the laser beam (Figure S2), CFD simulations of a 3 μm bubble (Figure S3), trapping processes of the 540 nm and 0.96 μm PS beads (Figure S4), bubble expansion and shrinkage process (Figure S5), generation of two microbubbles (Figure S6), patterning of 540 nm PS beads using 1 μm bubble (Figure S7), comparison between natural convection and bubble patterning (Figure S8), SEM of the 3D hollow structure with 60 nm PS beads (Figure S9), CFD simulations on the 3D hollow structure with 60 nm PS beads (Figure S10), continuous writing of 60 nm PS beads (Figure S11) and lifetime measurement of the CdSe/ZnS quantum dots on the glass substrate (Figure S12) (PDF)

Movie 1: real-time trapping (AVI)

Movie 2: expansion of the microbubble (AVI)

Movie 3: shrinkage of the microbubble (AVI)

Movie 4: real-time continuous writing process (AVI)

Movie 5: comparison between the natural convection before the bubble generation and the trapping and patterning of a 0.96 μm PS bead after the formation of the microbubble (AVI)

AUTHOR INFORMATION

Corresponding Author

*E-mail: zheng@austin.utexas.edu.

Author Contributions

$^{\nabla}$L.L and X.P contributed equally to this paper.

Notes

The authors declare no competing financial interest.

ACKNOWLEDGMENTS

The authors acknowledge the financial support of the Beckman Young Investigator Program and the Texas Advanced Computing Center (TACC) at The University of Texas at Austin for providing HPC resources that have contributed to the research results reported within this paper. URL: http://www.tacc.utexas.edu. We thank M. Wang, and Z. Wu for helpful discussions on the results and proofreading the manuscript.

REFERENCES

(1) Ito, T.; Okazaki, S. *Nature* **2000**, *406*, 1027−1031.

(2) Huo, F.; Zheng, G.; Liao, X.; Giam, L. R.; Chai, J.; Chen, X.; Shim, W.; Mirkin, C. A. *Nat. Nanotechnol.* **2010**, *5*, 637−640.

(3) Ozel, T.; Bourret, G. R.; Mirkin, C. A. *Nat. Nanotechnol.* **2015**, *10*, 319−324.

(4) Geissler, M.; Xia, Y. N. *Adv. Mater.* **2004**, *16*, 1249−1269.

(5) Rycenga, M.; Cobley, C. M.; Zeng, J.; Li, W.; Moran, C. H.; Zhang, Q.; Qin, D.; Xia, Y. *Chem. Rev.* **2011**, *111*, 3669−3712.

(6) Wang, X.; Zhuang, J.; Peng, Q.; Li, Y. *Nature* **2005**, *437*, 121−124.

(7) Wiley, B.; Sun, Y.; Xia, Y. *Acc. Chem. Res.* **2007**, *40*, 1067−1076.

(8) Xia, Y.; Yang, P.; Sun, Y.; Wu, Y.; Mayers, B.; Gates, B.; Yin, Y.; Kim, F.; Yan, H. *Adv. Mater.* **2003**, *15*, 353−389.

(9) Dahl, M.; Liu, Y.; Yin, Y. *Chem. Rev.* **2014**, *114*, 9853−9889.

(10) Rabani, E.; Reichman, D. R.; Geissler, P. L.; Brus, L. E. *Nature* **2003**, *426*, 271−274.

(11) Hulteen, J. C.; Treichel, D. A.; Smith, M. T.; Duval, M. L.; Jensen, T. R.; Van Duyne, R. P. *J. Phys. Chem. B* **1999**, *103*, 3854−3863.

(12) Haynes, C. L.; Van Duyne, R. P. *J. Phys. Chem. B* **2001**, *105*, 5599−5611.

(13) Lu, Y.; Yin, Y.; Li, Z.-Y.; Xia, Y. *Nano Lett.* **2002**, *2*, 785−788.

(14) Xia, Y.; Yin, Y.; Lu, Y.; McLellan, J. *Adv. Funct. Mater.* **2003**, *13*, 907−918.

(15) Tao, A.; Sinsermsuksakul, P.; Yang, P. *Nat. Nanotechnol.* **2007**, *2*, 435−440.

(16) Piner, R. D.; Zhu, J.; Xu, F.; Hong, S.; Mirkin, C. A. *Science* **1999**, *283*, 661−663.

(17) Salaita, K.; Wang, Y.; Mirkin, C. A. *Nat. Nanotechnol.* **2007**, *2*, 145−155.

(18) Huo, F.; Zheng, Z.; Zheng, G.; Giam, L. R.; Zhang, H.; Mirkin, C. A. *Science* **2008**, *321*, 1658−1660.

(19) Ahn, J.-H.; Kim, H.-S.; Lee, K. J.; Jeon, S.; Kang, S. J.; Sun, Y.; Nuzzo, R. G.; Rogers, J. A. *Science* **2006**, *314*, 1754−1757.

(20) Grier, D. G. *Nature* **2003**, *424*, 810−816.

(21) Pauzauskie, P. J.; Radenovic, A.; Trepagnier, E.; Shroff, H.; Yang, P.; Liphardt, J. *Nat. Mater.* **2006**, *5*, 97−101.

(22) Selhuber-Unkel, C.; Zins, I.; Schubert, O.; Sönnichsen, C.; Oddershede, L. B. *Nano Lett.* **2008**, *8*, 2998−3003.

(23) Wilson, B. K.; Hegg, M.; Miao, X.; Cao, G.; Lin, L. Y. *Opt. Express* **2008**, *16*, 17276−17281.

(24) Nedev, S.; Urban, A. S.; Lutich, A. A.; Feldmann, J. *Nano Lett.* **2011**, *11*, 5066−5070.

(25) Chiou, P. Y.; Ohta, A. T.; Wu, M. C. *Nature* **2005**, *436*, 370−372.

(26) Wu, M. C. *Nat. Photonics* **2011**, *5*, 322−324.

(27) Huang, K.-W.; Wu, Y.-C.; Lee, J.-A.; Chiou, P.-Y. *Lab Chip* **2013**, *13*, 3721−3727.

(28) Huang, K.-W.; Su, T.-W.; Ozcan, A.; Chiou, P.-Y. *Lab Chip* **2013**, *13*, 2278−2284.

(29) Jamshidi, A.; Neale, S. L.; Yu, K.; Pauzauskie, P. J.; Schuck, P. J.; Valley, J. K.; Hsu, H.-Y.; Ohta, A. T.; Wu, M. C. *Nano Lett.* **2009**, *9*, 2921−2925.

(30) Hu, W.; Ishii, K. S.; Fan, Q.; Ohta, A. T. *Lab Chip* **2012**, *12*, 3821−3826.

(31) Hashmi, A.; Yu, G.; Reilly-Collette, M.; Heiman, G.; Xu, J. *Lab Chip* **2012**, *12*, 4216−4227.

(32) Zhao, C.; Xie, Y.; Mao, Z.; Zhao, Y.; Rufo, J.; Yang, S.; Guo, F.; Mai, J. D.; Huang, T. J. *Lab Chip* **2014**, *14*, 384−391.

(33) Fang, Z.; Zhen, Y.-R.; Neumann, O.; Polman, A.; García de Abajo, F. J.; Nordlander, P.; Halas, N. J. *Nano Lett.* **2013**, *13*, 1736−1742.

(34) Neumann, O.; Urban, A. S.; Day, J.; Lal, S.; Nordlander, P.; Halas, N. J. *ACS Nano* **2013**, *7*, 42−49.

(35) Baffou, G.; Polleux, J.; Rigneault, H.; Monneret, S. *J. Phys. Chem. C* **2014**, *118*, 4890−4898.

(36) Baral, S.; Green, A. J.; Livshits, M. Y.; Govorov, A. O.; Richardson, H. H. *ACS Nano* **2014**, *8*, 1439−1448.

(37) Raut, H. K.; Dinachali, S. S.; Loke, Y. C.; Ganesan, R.; Ansah-Antwi, K. K.; Góra, A.; Khoo, E. H.; Ganesh, V. A.; Saifullah, M. S. M.; Ramakrishna, S. *ACS Nano* **2015**, *9*, 1305−1314.

(38) Wu, D.; Wang, J.-N.; Niu, L.-G.; Zhang, X. L.; Wu, S. Z.; Chen, Q.-D.; Lee, L. P.; Sun, H. B. *Adv. Opt. Mater.* **2014**, *2*, 751−758.

(39) Serra, F.; Gharbi, M. A.; Luo, Y.; Liu, I. B.; Bade, N. D.; Kamien, R. D.; Yang, S.; Stebe, K. J. *Adv. Opt. Mater.* **2015**, *3*, 1287−1292.

(40) Liu, N.; Tang, M. L.; Hentschel, M.; Giessen, H.; Alivisatos, A. P. *Nat. Mater.* **2011**, *10*, 631−636.

(41) Wood, D. K.; Weingeist, D. M.; Bhatia, S. N.; Engelward, B. P. *Proc. Natl. Acad. Sci. U. S. A.* **2010**, *107*, 10008−10013.

(42) Yan, R.; Simpson, J. R.; Bertolazzi, S.; Brivio, J.; Watson, M.; Wu, X.; Kis, A.; Luo, T.; Hight Walker, A. R.; Xing, H. G. *ACS Nano* **2014**, *8*, 986−993.

(43) Hoang, T. B.; Akselrod, G. M.; Argyropoulos, C.; Huang, J.; Smith, D. R.; Mikkelsen, M. H. *Nat. Commun.* **2015**, *6*, 7788.

(44) Johnson, P.; Christy, R. *Phys. Rev. B* **1972**, *6*, 4370−4379.

DOI: 10.1021/acs.nanolett.5b04524
Nano Lett. XXXX, XXX, XXX−XXX